Applied Surface Science 635 (2023) 157718

Contents lists available at ScienceDirect

Applied Surface Science

journal homepage: www.elsevier.com/locate/apsusc

Full Length Article

Tuning the lattice thermal conductivity of bilayer penta-graphene by interlayer twisting

Yanyan Chen [a], Chenxin Zhang [a], Jie Sun [a], Dongyuan Ni [a], Cunzhi Zhang [b], Qian Wang [a,*]

[a] School of Materials Science and Engineering, CAPT, BKL-MEMD, Peking University, Beijing 100871, China
[b] Pritzker School of Molecular Engineering, University of Chicago, Chicago, IL 60636.87, United States

ARTICLE INFO

Keywords:
Interlayer twisting
Penta-graphene
Thermal conductivity
Four-phonon scattering
Two-channel transport

ABSTRACT

Penta-graphene (PG) is the well-known prototype of the extensively studied 2D pentagon-based materials in recent years, and twisting strategy has been widely used to tune the properties of 2D sheets since the discovery of superconductivity in twisted bilayer graphene. However, no study is reported on how twisting affects the phonon properties of such penta-sheets. In this work, for the first time, we study the effect of twisting on the phonon transport properties of PG by using density functional theory and the phonon Boltzmann transport equation combined with two-channel transport theory and machine learning method. It is found that the in-plane lattice thermal conductivity of the twisted bilayer PG with a twist angle of 36.87° is only 96.72 W/mK at 300 K, reduced by 77.16% as compared to that of untwisted bilayer PG, and the four-phonon interaction further reduces the thermal conductivity by nearly 36%, while the coherence contribution to the thermal conductivity is enhanced to 9.69 W/mK from 0.13 W/mK by twisting. These results indicate that interlayer twisting not only can enhance three- and four-phonon scattering but also can uplift phonon coherence due to the resulted complex atomic configuration and high anharmonicity in bilayer PG.

1. Introduction

Graphene [1] and penta-graphene (PG) [2,3] are two well-known two-dimensional (2D) carbon allotropes with exotic properties. In particular, the superconductivity with transition temperature of 1.7 K was observed in twisted bilayer graphene (T-BG) with an angle of 1.1° between the two layers [4]. This experimental breakthrough has led to an emerging field called twistronics, which studies how twist angle (θ) between the two layers of a 2D material modifies the electronic [4–6], optical [7–10], and magnetic properties [11,12]. In recent years, it has been demonstrated that twisting offers a new strategy of tuning material properties going beyond the conventional doping, alloying, strain engineering, etc. However, as compared to the rapid development of twistronics, the studies on phonon transport properties of twisted materials are very limited, although phonon-related properties of a material are equally important as the other properties. In fact, twisting provides a unique platform to realize the anti-Slack criteria [13] for low thermal conductivity because interlayer twisting would result in a more complex crystal structure with lower symmetry, smaller Brillouin zone, and more complex bonding as compared to its untwisted counterpart, which would effectively reduce the lattice thermal conductivity (κ). For example, it was found that the κ of T-BG with a twist angle of 2° is reduced by 15% at 320 K [14], and the κ of the suspended T-BG near room temperature is lowered by 25.49% as compared to that of AB stacking bilayer graphene due to the effect of interlayer rotation on phonon dispersion relation [15].

On the other hand, PG emerges as a rising star in the field of 2D materials due to its unique geometry and novel physical properties, thus, it has been extensively studied and has led to a new field of pentagonal 2D materials [3,16]. The properties of PG are very different from those of graphene resulting from the completely different structural units, the five-membered and six-membered rings, respectively. For instance, the κ of PG is 255 ~ 645 W/mK [17,18], which is much smaller than that of graphene (2434 ~ 4120 W/mK) [19–21], and the κ of bilayer PG is 592 W/mK [22], which is also significantly reduced as compared to the value of 1896 W/mK for bilayer graphene [15]. However, to the best of our knowledge, the influence of twisting on the κ of PG has not yet been reported. Studying how twisting affects the thermal transport of PG not only sheds light on better understanding the 2D pentagonal carbon, but also provides an example for studying other penta-sheets especially the

* Corresponding author.
E-mail address: qianwang2@pku.edu.cn (Q. Wang).

https://doi.org/10.1016/j.apsusc.2023.157718
Received 12 October 2022; Received in revised form 29 May 2023; Accepted 4 June 2023
Available online 8 June 2023

experimentally synthesized ones including penta-$PdSe_2$ [23], penta-NiN_2 [24] and penta-PdS_2 [25]. This motivates us to carry out this study.

2. Computational methods

Our calculations are based on density functional theory (DFT) as implemented with the Vienna *ab initio* simulation package (VASP) [26]. The projector augmented wave (PAW) method [27,28] is used to treat the rapidly oscillating wavefunctions near the ion cores with the cutoff of 500 eV. The Perdwe-Burke-Ernzerhof (PBE) [29] functional within the generalized gradient approximation (GGA) [30] is employed for the exchange correlation potential of electrons, and optB88-vdW functional [31,32] is applied for dispersion force. A vacuum space of 16.21 Å in the out of plane direction is used. During geometry optimization, the Monkhorst-Pack [33] *k*-point with a grid density of $2\pi \times 0.02$ Å^{-1} are used to sample the Brillouin zone for integration in the reciprocal space and the convergence criteria for the total energy and atomic force calculations are taken as 1×10^{-6} eV and 1×10^{-4} eV/Å, respectively.

According to the two-channel transport theory [34] and the unified theory [35], the total lattice thermal conductivity κ_L is composed of the phonon contribution κ_L^p and the coherence contribution κ_L^c, namely, $\kappa_L = \kappa_L^p + \kappa_L^c$, here κ_L^p is related to the particle-like propagation of phonon wavepackets (the populations' contribution) discussed by Boltzmann transport equation (BTE) [36], and κ_L^c is associated with the wave-like tunneling (the coherence contribution) described by the unified theory [35]. Specifically, κ_L^p is dominated by phonons in semiconductors, and can be expressed as

$$\kappa_{L,\alpha\beta}^p = \frac{1}{N}\sum_{\lambda} C_\lambda \nu_{\alpha,\lambda}\nu_{\beta,\lambda}\tau_\lambda$$

where α and β denote Cartesian indices, λ is the phonon mode, and N is the volume of a unit cell. C is the heat capacity, ν is the phonon group velocity and τ is the phonon lifetime. The contribution of three-phonon interactions to κ_L^p can be calculated by solving the BTE via an iterative scheme as implemented in the ShengBTE package [37], while, due to the complex lattice structure, the four-phonon scattering rates are only computed at the relaxation time approximation (RTA) level, being used as the input of the iterative scheme to determine the nonequilibrium phonon distributions, as did in previous study [38]. The inputs for the calculation of κ_L^p are the harmonic (second order) and anharmonic (third and fourth order) interatomic force constants (IFCs). The harmonic IFCs are obtained by using the finite displacement method implemented in Phonopy code [39], while the anharmonic IFCs are efficiently extracted by training a force constants potential (FCP) based on a DFT dataset containing 100 configurations with random atomic displacements of 0.01 Å generated by the Monto Carlo rattle method using the HIPHIVE package [40–42]. The *k*-meshes of $2 \times 2 \times 1$ and $3 \times 3 \times 1$ are chosen to calculate the interatomic forces during the high-accuracy first-principles calculations for T-BPG and bilayer PG, respectively. The atomic forces and total energy are collected as training dataset for machine learning, and the associated parameters are trained based on the training dataset by solving a set of linear equations using the least-squares fitting method. To balance the calculation accuracy and computational cost, the second, third and fourth order cutoff distances are set to 6.00, 4.00, and 3.00 Å for T-BPG, and the corresponding values for bilayer PG are set to 5.00, 4.00, and 3.00 Å, respectively. The goodness of fit (R^2) of training set and test set for T-BPG (bilayer PG) is 0.9999853 (0.9999113) and 0.9998155 (0.99989), respectively, showing the accuracy of the fitted interatomic forces. Finally, the three- and four-phonon scattering rates and κ_L^p are calculated using these IFCs data in the ShengBTE package. The *q*-point meshes adopted for solving κ_L^p without (κ_L^3) and with (κ_L^{3+4}) four-phonon scattering processes are $16 \times 16 \times 1$ and $6 \times 6 \times 1$ for T-BPG, respectively, and the corresponding *q*-point meshes are $91 \times 91 \times 1$ and $15 \times 15 \times 1$ for bilayer PG. The thickness of 8.89 and 8.41 Å are used for T-BPG and bilayer PG during the solution of lattice thermal conductivity, which is obtained by calculating the sum of the upper and lower van der Waals (vdW) radii [43]. On the other hand, κ_L^c can be derived from the equation for the coherences [35]:

$$\kappa_{L,\alpha\beta}^c = \frac{\hbar^2}{k_B T^2}\frac{1}{VN_c}\sum_q\sum_{s\neq s'}\frac{w(q)_s + w(q)_{s'}}{2}v^\alpha(q)_{s,s'}v^\beta(q)_{s,s'} \times \frac{w(q)_s\overline{N}(q)_s(\overline{N}(q)_s+1) + w(q)_{s'}\overline{N}(q)_{s'}(\overline{N}(q)_{s'}+1)}{4(w(q)_s - w(q)_{s'})^2 + (\Gamma(q)_s + \Gamma(q)_{s'})^2} \times (\Gamma(q)_s + \Gamma(q)_{s'})$$

in which $\hbar$, k_B, T, N_c are the reduced Plank constant, Boltzmann constant, temperature and number of phonon wave vectors. $w(q)_s$ and $\Gamma(q)_s$ are the frequency and phonon scattering rates indexed by wave vector q with the branch s, respectively, and $\overline{N}(q)_s$ is the equilibrium Bose-Einstein distribution. The $w(q)_s$ is given by the second order IFCs, and phonon scattering rates $\Gamma(q)_s$ is obtained by including the three-phonon scattering rates (τ_3^{-1}) and four-phonon scattering rates (τ_4^{-1}): $\Gamma(q)_s = \tau_3^{-1} + \tau_4^{-1}$. In addition, $v(q)_{s,s'}$ is the off-diagonal velocity matrix, which can be obtained by the following equation:

$$v(q)_{s,s'} = \frac{1}{\omega(q)_s + \omega(q)_{s'}}\langle e(q)_s\left|\frac{\partial D(q)}{\partial q}\right|e(q)_{s'}\rangle,$$

where $e(q)_s$ is the eigenvector of the phonon mode s, and $D(q)$ is the dynamical matrix of the crystal with an eigenvalue of $\omega^2(q)_s$. The off-diagonal velocity matrix is calculated by using the dynamical matrix solver implemented in ShengBTE, and the *q*-meshes are set as the same as those for the calculations of populations' contribution ($6 \times 6 \times 1$ for T-BPG and $15 \times 15 \times 1$ for bilayer PG). Finally, combining the calculated phonon scattering rates, phonon dispersion and off-diagonal velocity matrix, the κ_L^c is calculated based on the coherence's equation with our in-house code.

3. Results and discussions

3.1. Geometric structure and stability

We begin with the AA stacking bilayer PG as the AA stacking was found to be the stable stacking pattern for untwisted bilayer PG [22]. The twisted PG structures are obtained by using the CellMatch code [44]. We find that the interlayer twisting generates large size unit cells with reduced symmetry. For instance, the unit cells with small twist angles $\theta = 5^\circ$ and 10° contain 2172 and 732 atoms, respectively. The number of atoms per unit cell as a function of twist angle θ is given in Fig. S1 in the Support Information (SI). Considering both twisting effect and computational cost, we choose the twisted bilayer PG (T-BPG) with an angle of 36.87° for further investigation as its corresponding unit cell has the highest symmetry and the least number of atoms among all the twisted structures, as shown in Fig. 1. The crystal structure of the T-BPG sheet with this specific angle has a tetragonal lattice with the lattice constants $a = b = 8.12$ Å and the space group $C222$ (No. 21). We note that the fourfold inversion symmetry of the bilayer PG is broken after twisting, enhancing the structural anharmonicity, and the interlayer distance increases from 2.56 Å of the bilayer PG to 3.08 Å of the T-BPG, showing that twist also modulates the interlayer potential and interactions.

To examine the stability of the T-BPG structure, we first calculate its phonon spectrum. As shown in Fig. 2(a), the absence of imaginary modes in the entire Brillouin zone confirms that T-BPG is dynamically stable. To investigate the effect of twisting on the phonon vibration modes, we also plot the phonon spectrum of the untwisted bilayer PG in Fig. 2(a). One can see the softening of the low-frequency phonon branches in T-BPG, especially for the acoustic branches, i.e. the flexural

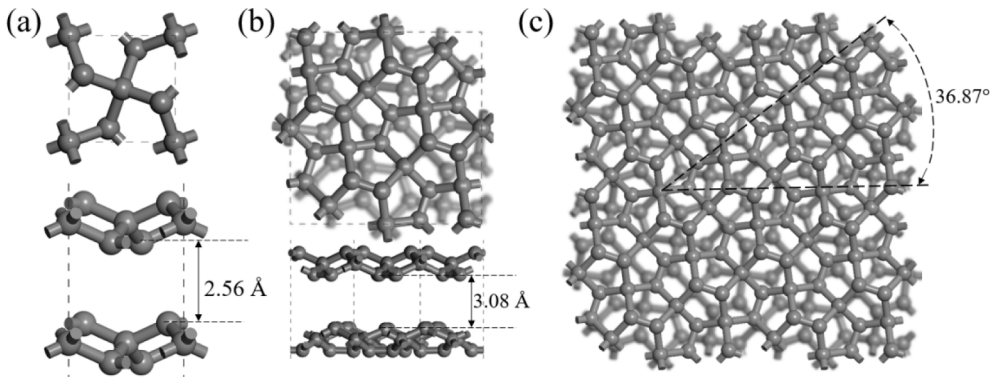

Fig. 1. (a) Unit cell of the bilayer PG, and (b) the T-BPG with $\theta = 36.87^{\circ}$. (c) Top view of the T-BPG superlattice ($2 \times 2 \times 1$).

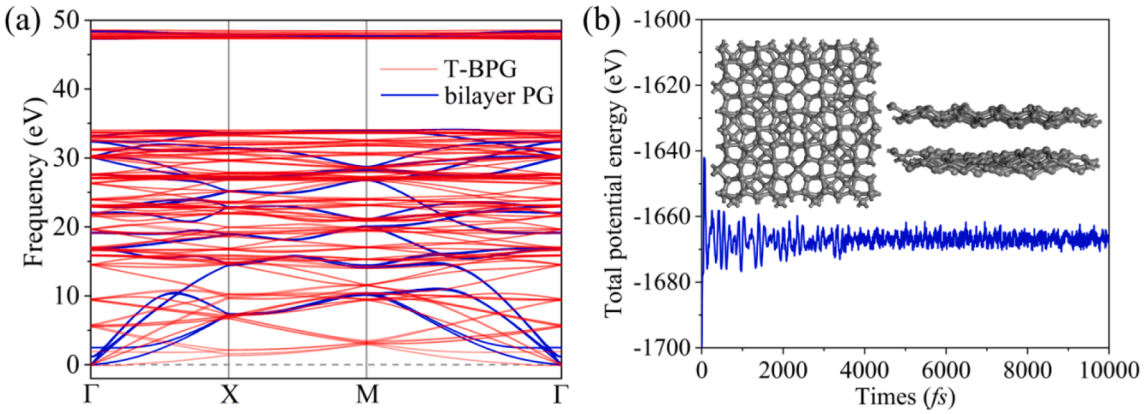

Fig. 2. (a) Phonon spectra of the T-BPG and bilayer PG. (b) Total potential energy fluctuation during AIMD simulation of T-BPG at 1000 K. The insets show the snapshot of the atomic configuration of T-BPG at the end of the AIMD simulation.

acoustic (ZA) mode that characterizes the out-of-plane vibration of atoms becomes almost flat near the Γ point after twisting, as is the case with the twisted Bi_2O_2Se [45], and the softening of phonon branches usually results in low phonon group velocity. In addition, in the twisted system, there are more overlap between the acoustic and the low-lying optical phonon modes (below 15 THz), which would induce stronger phonon scattering phase space and phonon couplings, as found in previous study [46].

We then study the thermal stability of T-BPG by performing the *ab initio* molecular dynamics (AIMD) simulations with the canonical ensemble. A $2 \times 2 \times 1$ supercell containing 240 atoms is used to minimize the constraint of the periodic boundary conditions. We perform the simulations at 300, 500, 700 and 1000 K, and plot the results at 1000 K in Fig. 2(b). The total energy fluctuates around a constant value, and the structural skeleton of T-BPG has no obvious distortions after heated for 10 picosecond (*ps*) with a time step of 1 fs (*fs*). These results suggest that T-BPG is thermally stable at room temperature and can withstand high temperatures up to 1000 K.

We further calculate the elastic constants of the T-BPG to verify its mechanical stability. For this 2D tetragonal lattice, there are three non-zero and independent elastic constants, i.e. C_{11}, C_{12} and C_{66}, which are calculated by fitting the second order polynomial to the change of the total energy versus applied strain using the VASPKIT code [47]. The calculated values are $C_{11} = 348.01$ N/m, $C_{12} = -31.28$ N/m and $C_{66} = 186.25$ N/m, which are fully satisfy the Born-Huang criteria [48], namely, $C_{11} > 0$, $C_{66} > 0$ and $C_{11} > C_{12}$. Therefore, the T-BPG structure is mechanically stable. Interestingly, we find that the C_{12} is negative for this nanosheet, leading to a negative Poisson's ratio of -0.09, showing that twisting with an angle of 36.87° does not change the unique mechanical properties of PG [2], namely, it possesses a negative Poisson's ratio. Therefore, T-BPG is also a promising auxetic material for nanomechanical devices.

3.2. Electronic properties

To investigate the electronic properties of T-BPG, we calculate its electronic band structure at the PBE level due to the large unit cell of the T-BPG structure, and plot the calculated results in Fig. 3. For comparison, we also carry out the calculations for the bilayer PG and PG, and present the results in Fig. 3 as well. One can see that the band gap of T-BPG is reduced to 0.76 eV from 1.95 eV of the twist-free bilayer PG. Considering the fact that T-BPG is semiconducting, phonons dominate the thermal transport. Therefore, we focus on the study of the lattice thermal conductivity κ_L to explore the effect of twisting on phonon properties.

3.3. Three-phonon scattering processes

The lattice thermal conductivity κ_L^3 of T-BPG is calculated via the BTE theory by considering three-phonon scattering processes. As shown in Fig. 4(a), the in-plane κ_L^3 of T-BPG is only 96.72 W/mK at 300 K, reduced by 77.16% with respect to that of the bilayer PG (423.43 W/mK). When the temperature increases to 1000 K, the κ_L^3 of T-BPG and bilayer PG is 29.10 and 90.04 W/mK, respectively, exhibiting a significant reduction of 67.68% and showing the importance of twisting on modulating κ_L^3 of PG system again. And both the T-BPG and bilayer PG exhibit the temperature dependence close to $1/T$, suggesting that the anharmonic phonon–phonon interactions are dominant in phonon scattering mechanism. The spectral contributions of phonon modes to κ_L^3 at 300 K are presented in Fig. 4(b), showing that the κ_L^3 mainly contributes from

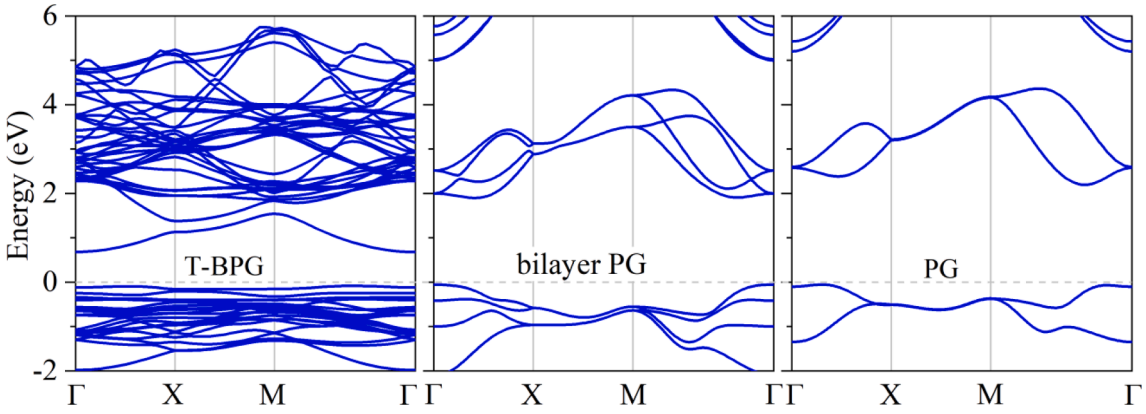

Fig. 3. Band structures of the T-BPG, bilayer PG and PG.

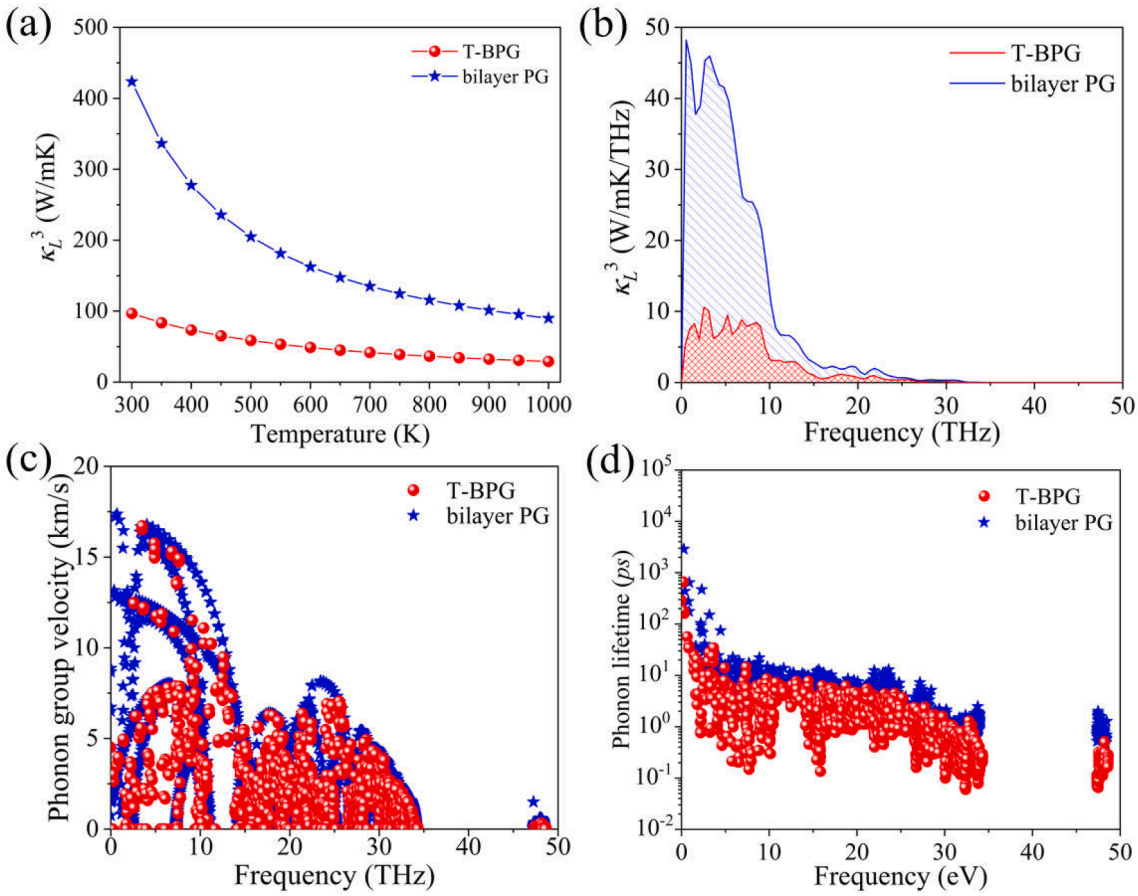

Fig. 4. (a) Temperature dependent κ_L^3, (b) spectral contributions to κ_L^3, (c) phonon group velocity and (d) phonon lifetime with the change of frequency of T-BPG and bilayer PG, respectively.

phonons with their frequencies lower than 15 THz in both the twisted and untwisted bilayer PG.

To understand the underlying mechanism, we study the change of the specific heat capacity C at constant volume, phonon group velocity v and phonon lifetime τ of the bilayer PG after twisting, which are the three important parameters determining the κ_L^3, to find out the main reason for the reduced κ_L^3 in T-BPG. The specific heat capacity C of T-BPG and bilayer PG at 300 K is 1.56×10^6 and 1.65×10^6 J/m^{3}K, respectively, suggesting that twisting reduces the specific heat capacity which would result in a reduced lattice thermal conductivity. Since twisting leads to the softening of acoustic branches, the low phonon group velocity in T-BPG is expected. As shown in Fig. 4(c), the twisted PG possesses lower phonon group velocity in the whole frequency region, as compared with that of untwisted PG. For quantitative analysis, here we calculate the average phonon group velocity based on the phonons with their frequencies lower than 15 THz. The average phonon group velocity of T-BPG is 3.79 km/s, while the corresponding value of bilayer PG is 5.29 km/s. Thus, the squared average phonon group velocity of T-BPG is further calculated to be 49% lower than that of bilayer PG. The difference in their phonon velocities partially contributes to the reduced κ_L^3 in T-BPG. Another factor for the reduced thermal conductivity is the phonon lifetime, which is the inversion of the phonon scattering rates. As shown in Fig. 4(d), the phonon lifetime of T-BPG is significantly

suppressed by an order of magnitude compared to that of bilayer PG. In the low frequency region (below 15 THz), the phonon lifetime decreases almost from 10^2 to 10^0 *ps* for T-BPG with the increasing frequency, while for the bilayer PG, the phonon lifetime changes almost from 10^3 to 10^1 *ps*. It can be inferred that the reduced phonon lifetime is the main reason for the reduced κ_L^3 in T-BPG.

To further explore how the interlayer twisting affects the anharmonic interactions, the Grüneisen parameter (γ) and weighted three-phonon scattering phase space (WP3) [49] are calculated, which are used to quantitatively assess the strength and possibilities of anharmonic scatterings. The Grüneisen parameter of T-BPG and bilayer PG at 300 K is −0.36 and −0.14, respectively, indicating that twisting significantly enhances the anharmonicity. This phenomenon is consistent with our cognition that materials with low symmetry and complex unit cell usually possess strong anharmonicity. The calculated results of WP3 of the twisted PG are presented in Fig. S2, which is almost two order of magnitude larger than that of the untwisted PG. The enhanced γ and WP3 originate from the complex geometric structure with lower symmetry and more complex phonon dispersion relations resulting from the twist, eventually leading to the low thermal conductivity.

3.4. Four-phonon scattering processes

To get more accurate thermal conductivity, we further calculate κ_L by including four-phonon scattering. Generally, the scattering processes including four-phonon interaction can allow more phonon scattering channels, leading to a reduction in total thermal conductivity, especially in materials with ultralow lattice thermal conductivity [46,50], large acoustic-optical phonon band gap [38,51], or reflection symmetry [52,53]. However, one of the key steps during the calculation of four-phonon scattering processes is to obtain the accurate fourth order IFCs, which is time consuming and computationally expensive. For example, due to the low symmetry and complex structure of T-BPG with 60 atoms in its unit cell, there are about 34,424 DFT calculations required to compute the fourth order IFCs by using the finite displacement method. Therefore, machine learning method is used to generate the anharmonic IFCs as mentioned previously.

To study the effect of four-phonon scattering, the lattice thermal conductivity κ_L^{3+4} and phonon scattering rates τ_4^{-1} of T-BPG with including four-phonon scattering processes are calculated. As shown in Table 1, the κ_L^{3+4} of T-BPG is 62.33 W/mK at 300 K, reduced by 35.56% as compared to the value of κ_L^3, while the κ_L^{3+4} of bilayer PG is reduced by 27.53%. These reductions show an important effect of four-phonon scattering processes on the thermal conductivity of T-BPG and bilayer PG, different from that in graphene and penta-NiN_2, where the κ_L^{3+4} reduces by 76.06% [52] and 89.32% [53], respectively. The underlying reason for the dramatic decrease of κ_L^{3+4} in graphene and penta-NiN_2 is related to the reflection symmetry of the planar sheets, which forbids the scattering processes with odd number of ZA modes [52,53]. However, the structure of PG is buckled, and the selection rule has less effect. In addition, the four-phonon scattering rates τ_4^{-1} and the four-phonon scattering phase space WP4 of T-BPG at 300 K are plotted in Fig. 5(a) and Fig. S3. The four-phonon scattering rates and four-phonon weighted phase space are quite high, especially in the low frequency range of 0–10 THz, showing promising scattering channels for four-phonon processes.

Table 1
Thermal conductivity (in W/mK) of the T-BPG and bilayer PG calculated at different mechanisms and different temperatures.

	κ_L^3	κ_L^{3+4}	κ_L^c	κ_L^{3+4+c}
T-BPG (300 K)	96.72	62.33	9.69	72.02
bilayer PG (300 K)	423.43	306.86	0.13	306.99
T-BPG (1000 K)	29.10	14.79	6.23	21.02
bilayer PG (1000 K)	90.04	57.95	0.79	58.74

Moreover, as temperature increases to 1000 K, the κ_L^{3+4} of T-BPG is only 14.79 W/mK as listed in Table 1. The κ_L^{3+4} is reduced by 49.18% and 35.64% with the increasing temperature for T-BPG and bilayer PG, respectively, indicating that the four-phonon scattering becomes much more important when temperature increases. This phenomenon can be explained by comparing the three-phonon and four-phonon scattering rates of T-BPG and bilayer PG at 300 and 1000 K. As shown in Fig. 5(a) and 5(b), the τ_4^{-1} is increasing faster than the τ_3^{-1} for T-BPG, and this leads to the enhanced importance of four-phonon scattering when temperature increases. This phenomenon is also observed for twist-free bilayer PG as shown in Fig. 5(c) and 5(d). These results have clearly indicated that the interlayer twisting can enhance three- and four-phonon scattering in the twisted system.

3.5. Coherence contribution to the thermal conductivity

The two-channel transport theory of thermal transport takes into account both diagonal and off-diagonal terms of the heat-flux operator, namely, the contributions from both phonon and the coherences. Previous studies have demonstrated that the coherence contribution to the thermal conductivity is non-ignorable in complex crystal with strong anharmonicity or disorder [54], such as cubic $Cu_{12}Sb_4S_{13}$ tetrahedrites [54] and 2D paraelectric SnSe [55]. Therefore, the coherence contribution to κ (κ_L^c) is further considered to correctly describe the thermal transport of T-BPG. Generally, the normal phonon modes with mean free path (MFP) greater than Ioffe-Regel limit [34] contribute to the κ_L^p and the diffusion-like "phonon" modes with MFP below the limit contribute to the κ_L^c, hence, we first calculate the phonon MFP Λ through $\Lambda = v\tau$ based on the phonon group velocity v and phonon lifetime τ. The calculated results are plotted in Fig. 6. The minimum interatomic spacing (Ioffe-Regel limit) in T-BPG and bilayer PG is 1.33 and 1.34 Å, respectively, and the MFP for almost every low-frequency phonon is larger than the limit, indicating weak coherence contribution for both T-BPG and bilayer PG.

As listed in Table 1, the κ_L^c for T-BPG is calculated to be 9.69 W/mK at 300 K, and only 13.45% of the total κ_L, while the κ_L^c for the twist-free bilayer PG is 0.13 W/mK at 300 K, 0.04% of total κ_L. Although the coherent term has a slight impact on the overall κ_L in both the bilayer PG and T-BPG because of their strong intrinsic phonon scatterings, the effect of twisting on coherence contribution is significant as the contribution from coherences is enhanced significantly when twisting is applied. Meanwhile, the κ_L^c of twisted bilayer PG increases from 0.13 to 9.69 W/mK, and from 0.79 to 6.23 W/mK for $T = 300$ and 1000 K respectively. These results have clearly indicated that the interlayer twisting not only can enhance three- and four-phonon scattering but also can uplift phonon coherence. By summing up three- and four-phonon scatterings and coherent thermal transport , the intrinsic thermal conductivity of twisted bilayer PG is found to be reduced to 72.02 W/mK from 306.99 W/mK at 300 K by interlayer twist angle of 36.87°, demonstrating the importance of interlayer twisting in tuning the lattice thermal conductivity of the PG system.

4. Conclusions

In this work, taking bilayer PG as an example, we demonstrate that twisting is an effective strategy for the tuning the κ_L of penta-sheets, going beyond hydrogenation [17], fluorination [56], strain engineering [57] and grain boundaries [58]. Different from the studies on the κ_L reported so far by only considering three-phonon scattering, we systematically study the thermal transport properties of the bilayer PG-based sheet by including three- and four-phonon scattering processes as well as the coherence contribution to heat with force constants fitted through machine learning. We find that from the bilayer PG to the T-BPG sheet, the in-plane κ_L is reduced from 423.43 to 96.72 W/mK at 300 K with only three-phonon scattering considered, and is further reduced

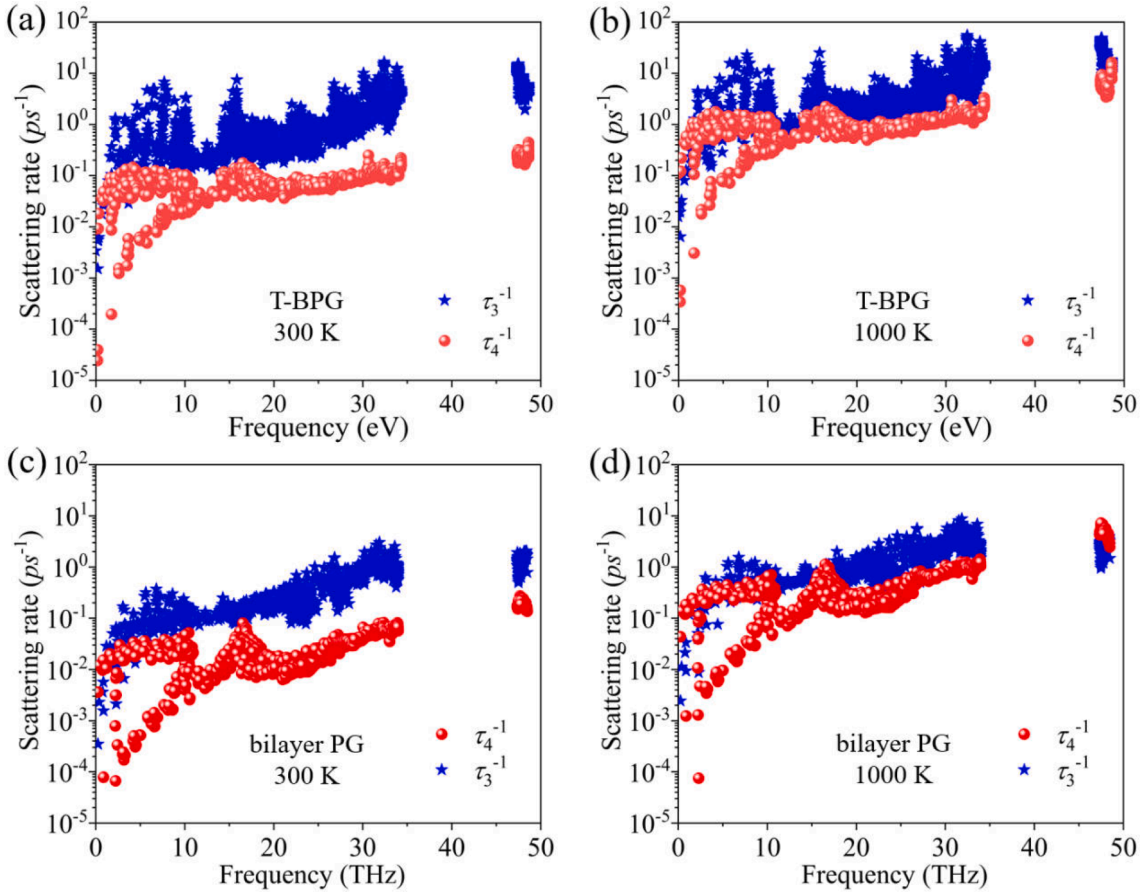

Fig. 5. Three-phonon and four-phonon scattering rates of T-BPG and bilayer PG at 300 and 1000 K.

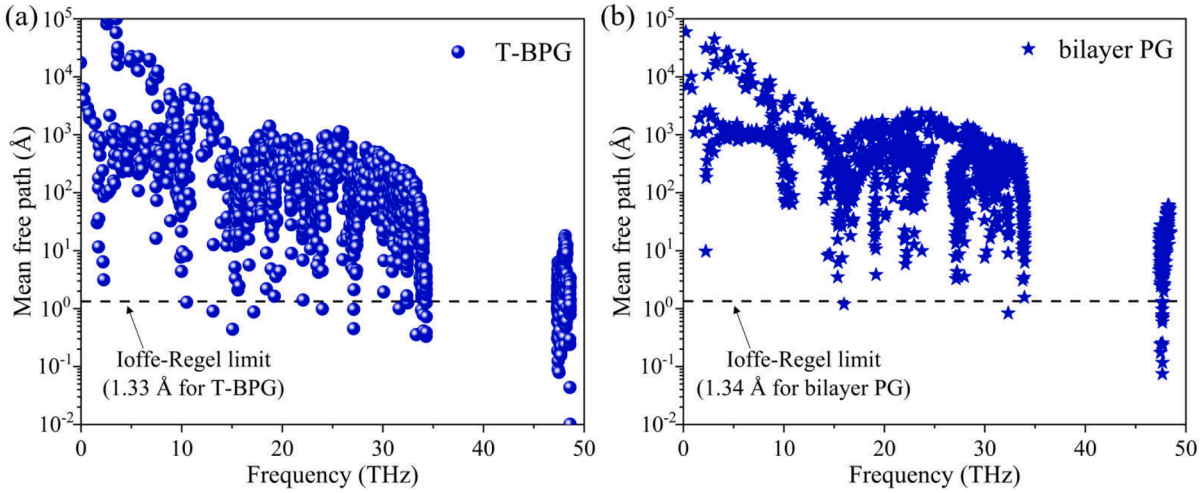

Fig. 6. Variation of the phonon mean free path with frequency for (a) T-BPG and (b) bilayer PG at 300 K. The horizontal line marks the Ioffe-Regel limit.

from 306.86 to 62.33 W/mK when four-phonon scattering is included, corresponding to a reduction of 77.16% and 79.69%, respectively. While the contribution from the coherences to the κ_L is 9.69 W/mK, but that for the untwisted bilayer PG is only 0.13 W/mK, which is enhanced significantly by twisting. This study demonstrates that interlayer twisting is an effective way to reduce the κ_L of bilayer PG, and also shows the importance of the effect of four-phonon scattering processes and two-channel transport on such pentagon-based materials with complex structures, and the methods used in this work can be also applied to study other penta-sheets especially the experimentally synthesized ones, such studies would significantly deepen our understanding on how twisting affects the thermal transport in layered penta-sheet systems.

Associated Contents.

Supporting Information.

The Supporting Information is available for the optimized geometry of T-BPG, number of atoms per unit cell at different twist angles, the weighted three-phonon phase space of T-BPG and bilayer PG, weighted three-phonon and four-phonon phase space of T-BPG at 300 K.

CRediT authorship contribution statement

Yanyan Chen: Conceptualization, Writing – original draft, Methodology, Software, Formal analysis, Investigation, Data curation, Visualization. **Chenxin Zhang:** Conceptualization, Methodology, Software, Formal analysis, Writing – review & editing, Visualization. **Jie Sun:** Methodology, Formal analysis, Investigation. **Dongyuan Ni:** Methodology, Software, Investigation. **Cunzhi Zhang:** Methodology, Software, Investigation. **Qian Wang:** Conceptualization, Funding acquisition, Project administration, Software, Writing – review & editing, Validation, Resources, Supervision.

Declaration of Competing Interest

The authors declare that they have no known competing financial interests or personal relationships that could have appeared to influence the work reported in this paper.

Data availability

Data will be made available on request.

Acknowledgements

This work is partially supported by grants from the National Natural Science Foundation of China (Grant Nos. NSFC-12274007 and NSFC-11974028) and is also supported by the High Performance Computing Platform of Peking University, China.

Appendix A. Supplementary Material

Supplementary Material to this article can be found online at https://doi.org/10.1016/j.apsusc.2023.157718.

References

[1] K.S. Novoselov, A.K. Geim, S.V. Morozov, D. Jiang, Y. Zhang, S.V. Dubonos, I. V. Grigorieva, A.A. Firsov, Electric field effect in atomically thin carbon films, Science 306 (2004) 666.
[2] S. Zhang, J. Zhou, Q. Wang, X. Chen, Y. Kawazoe, P. Jena, Penta-graphene: A new carbon allotrope, Proc. Natl. Acad. Sci. 112 (8) (2015) 2372–2377.
[3] M.A. Nazir, A. Hassan, Y. Shen, Q. Wang, Research progress on penta-graphene and its related materials: Properties and applications, Nano Today 44 (2022) 101501.
[4] Y. Cao, V. Fatemi, S. Fang, K. Watanabe, T. Taniguchi, E. Kaxiras, P. Jarillo-Herrero, Unconventional superconductivity in magic-angle graphene superlattices, Nature 556 (2018) 43–50.
[5] M. Serlin, C.L. Tschirhart, H. Polshyn, Y. Zhang, J. Zhu, K. Watanabe, T. Taniguchi, L. Balents, A.F. Young, Intrinsic quantized anomalous Hall effect in a moiré heterostructure, Science 367 (2020) 900–903.
[6] M.H. Naik, M. Jain, Ultraflatbands and shear solitons in Moiré patterns of twisted bilayer transition metal dichalcogenides, Phys. Rev. Lett. 121 (2018) 266401.
[7] J. Yan, C. Ma, Y. Huang, G. Yang, Tunable control of interlayer excitons in WS_2/MoS_2 heterostructures via strong coupling with enhanced Mie resonances, Adv. Sci. 6 (2019) 1802092.
[8] N. Zhang, A. Surrente, M. Baranowski, D.K. Maude, P. Gant, A. Castellanos-Gomez, P. Plochocka, Moiré intralayer excitons in a $MoSe_2$/MoS_2 heterostructure, Nano Lett. 18 (12) (2018) 7651–7657.
[9] W.-T. Hsu, Z.-A. Zhao, L.-J. Li, C.-H. Chen, M.-H. Chiu, P.-S. Chang, Y.-C. Chou, W.-H. Chang, Second harmonic generation from artificially stacked transition metal dichalcogenide twisted bilayers, ACS Nano 8 (3) (2014) 2951–2958.
[10] P. Moon, M. Koshino, Optical absorption in twisted bilayer graphene, Phys. Rev. B 87 (2013) 205404.
[11] A.L. Sharpe, E.J. Fox, A.W. Barnard, J. Finney, K. Watanabe, T. Taniguchi, M. A. Kastner, D. Goldhaber-Gordon, Emergent ferromagnetism near three-quarters filling in twisted bilayer graphene, Science 365 (6453) (2019) 605–608.
[12] S. Chen, M. He, Y.-H. Zhang, V. Hsieh, Z. Fei, K. Watanabe, T. Taniguchi, D. H. Cobden, X. Xu, C.R. Dean, M. Yankowitz, Electrically tunable correlated and topological states in twisted monolayer–bilayer graphene, Nat. Phys. 17 (3) (2021) 374–380.
[13] G.A. Slack, Nonmetallic crystals with high thermal conductivity, J. Phys. Chem. Solids 34 (2) (1973) 321–335.
[14] S. Han, X. Nie, S. Gu, W. Liu, L. Chen, H. Ying, L.e. Wang, Z. Cheng, L.i. Zhao, S. Chen, Twist-angle-dependent thermal conduction in single-crystalline bilayer graphene, Appl. Phys. Lett. 118 (19) (2021) 193104.
[15] H. Li, H. Ying, X. Chen, D.L. Nika, A.I. Cocemasov, W. Cai, A.A. Balandin, S. Chen, Thermal conductivity of twisted bilayer graphene, Nanoscale 6 (22) (2014) 13402–13408.
[16] Y. Shen, Q. Wang, Pentagon-based 2D materials: Classification, properties and applications, Phys. Rep. 964 (2022) 1–42.
[17] X. Wu, V. Varshney, J. Lee, T. Zhang, J.L. Wohlwend, A.K. Roy, T. Luo, Hydrogenation of penta-graphene leads to unexpected large improvement in thermal conductivity, Nano Lett. 16 (2016) 3925–3935.
[18] F.Q. Wang, J. Yu, Q. Wang, Y. Kawazoe, P. Jena, Lattice thermal conductivity of penta-graphene, Carbon 105 (2016) 424–429.
[19] S. Yue, G. Qin, X. Zhang, X. Sheng, G. Su, M. Hu, Thermal transport in novel carbon allotropes with sp^2 or sp^3 hybridization: an *ab initio* study, Phys. Rev. B 95 (2017) 085207.
[20] L. Lindsay, D.A. Broido, N. Mingo, Diameter dependence of carbon nanotube thermal conductivity and extension to the graphene limit, Phys. Rev. B 82 (2010) 161402.
[21] S. Chen, Q. Wu, C. Mishra, J. Kang, H. Zhang, K. Cho, W. Cai, A.A. Balandin, R. S. Ruoff, Thermal conductivity of isotopically modified graphene, Nat. Mater. 11 (2012) 203–207.
[22] F.Q. Wang, J. Liu, X. Li, Q. Wang, Y. Kawazoe, Weak interlayer dependence of lattice thermal conductivity on stacking thickness of penta-graphene, Appl. Phys. Lett. 111 (2017) 192102.
[23] W.L. Chow, P. Yu, F. Liu, J. Hong, X. Wang, Q. Zeng, C. Hsu, C. Zhu, J. Zhou, X. Wang, J. Xia, J. Yan, Y. Chen, D. Wu, T. Yu, Z. Shen, H. Lin, C. Jin, B.K. Tay, Z. Liu, High mobility 2D palladium diselenide field-effect transistors with tunable ambipolar characteristics, Adv. Mater. 29 (2017) 1602969.
[24] M. Bykov, E. Bykova, A.V. Ponomareva, F. Tasnádi, S. Chariton, V.B. Prakapenka, K. Glazyrin, J.S. Smith, M.F. Mahmood, I.A. Abrikosov, A.F. Goncharov, Realization of an ideal cairo tessellation in nickel diazenide NiN_2: High-pressure route to pentagonal 2D materials, ACS Nano 15 (2021) 13539–13546.
[25] X. Zhang, G. Su, J. Lu, W. Yang, W. Zhuang, K. Han, X. Wang, Y. Wan, X. Yu, P. Yang, Centimeter-scale few-layer PdS_2: Fabrication and physical properties, ACS Appl. Mater. Interfaces 13 (36) (2021) 43063–43074.
[26] G. Kresse, J. Furthmüller, Efficient iterative schemes for *ab initio* total-energy calculations using a plane-wave basis set, Phys. Rev. B 54 (1996) 11169–11186.
[27] P.E. Blöchl, Projector augmented-wave method, Phys. Rev. B 50 (1994) 17953–17979.
[28] G. Kresse, D. Joubert, From ultrasoft pseudopotentials to the projector augmented-wave method, Phys. Rev. B 59 (1999) 1758–1775.
[29] J.P. Perdew, K. Burke, M. Ernzerhof, Generalized gradient approximation made simple, Phys. Rev. Lett. 77 (1996) 3865–3868.
[30] Y.F. Hu, C. Storey, Efficient generalized conjugate gradient algorithms, Part 2: Implementation, J. Optim. Theory Appl. 69 (1) (1991) 139–152.
[31] M. Dion, H. Rydberg, E. Schröder, D.C. Langreth, B.I. Lundqvist, Van der Waals density functional for general geometries, Phys. Rev. Lett. 92 (2004) 246401.
[32] J. Klimeš, D.R. Bowler, A. Michaelides, Van der Waals density functionals applied to solids, Phys. Rev. B 83 (2011) 195131.
[33] H.J. Monkhorst, J.D. Pack, Special points for Brillouin-zone integrations, Phys. Rev. B 13 (1976) 5188–5192.
[34] S. Mukhopadhyay, D.S. Parker, B.C. Sales, A.A. Puretzky, M.A. McGuire, L. Lindsay, Two-channel model for ultralow thermal conductivity of crystalline Tl_3VSe_4, Science 360 (2018) 1455–1458.
[35] M. Simoncelli, N. Marzari, F. Mauri, Unified theory of thermal transport in crystals and glasses, Nat. Phys. 15 (2019) 809–813.
[36] M. Omini, A. Sparavigna, An iterative approach to the phonon Boltzmann equation in the theory of thermal conductivity, Phys. B 212 (1995) 101–112.
[37] W. Li, J. Carrete, N.A. Katcho, N. Mingo, ShengBTE: A solver of the Boltzmann transport equation for phonons, Comput. Phys. Commun. 185 (2014) 1747–1758.
[38] T. Feng, L. Lindsay, X. Ruan, Four-phonon scattering significantly reduces intrinsic thermal conductivity of solids, Phys. Rev. B 96 (2017) 161201.
[39] A. Togo, I. Tanaka, First principles phonon calculations in materials science, Scr. Mater. 108 (2015) 1–5.
[40] F. Eriksson, E. Fransson, P. Erhart, The Hiphive package for the extraction of high-order force constants by machine learning, Adv. Theory Simul. 2 (2019) 1800184.
[41] A. Taheri, S. Pisana, C.V. Singh, Importance of quadratic dispersion in acoustic flexural phonons for thermal transport of two-dimensional materials, Phys. Rev. B 103 (2021) 235426.
[42] E. Fransson, F. Eriksson, P. Erhart, Efficient construction of linear models in materials modeling and applications to force constant expansions, Npj Comput. Mater. 6 (2020) 135.
[43] X. Wu, V. Varshney, J. Lee, Y. Pang, A.K. Roy, T. Luo, How to characterize thermal transport capability of 2D materials fairly? – Sheet thermal conductance and the choice of thickness, Chem. Phys. Lett. 669 (2017) 233–237.
[44] P. Lazić, Cell Match: Combining two unit cells into a common supercell with minimal strain, Comput. Phys. Commun. 197 (2015) 324–334.
[45] J. Sun, M. Hu, C. Zhang, L. Bai, C. Zhang, Q. Wang, Ultralow thermal conductivity of layered Bi_2O_2Se induced by twisting, Adv. Funct. Mater. 32 (2022) 2209000.
[46] Z. Zeng, C. Zhang, H. Yu, W. Li, Y. Pei, Y. Chen, Ultralow and glass-like lattice thermal conductivity in crystalline $BaAg_2Te_2$: Strong fourth-order anharmonicity and crucial diffusive thermal transport, Mater. Today Phys. 21 (2021) 100487.
[47] V. Wang, N. Xu, J. Liu, G. Tang, W. Geng, VASPKIT: A user-friendly interface facilitating high-throughput computing and analysis using VASP code, Comput. Phys. Commun. 267 (2021) 108033.
[48] Z. Wu, E. Zhao, H. Xiang, X. Hao, X. Liu, J. Meng, Crystal structures and elastic properties of superhard IrN_2 and IrN_3 from first principles, Phys. Rev. B 76 (2007) 054115.

[49] W. Li, N. Mingo, Ultralow lattice thermal conductivity of the fully filled skutterudite $YbFe_4Sb_{12}$ due to the flat avoided-crossing filler modes, Phys. Rev. B 91 (2015) 144304.
[50] Z. Zeng, C. Zhang, Y. Xia, Z. Fan, C. Wolverton, Y. Chen, Nonperturbative phonon scatterings and the two-channel thermal transport in Tl_3VSe_4, Phys. Rev. B 103 (2021) 224307.
[51] C. Jin, E.C. Regan, A. Yan, M. Iqbal Bakti Utama, D. Wang, S. Zhao, Y. Qin, S. Yang, Z. Zheng, S. Shi, K. Watanabe, T. Taniguchi, S. Tongay, A. Zettl, F. Wang, Observation of moiré excitons in WSe_2/WS_2 heterostructure superlattices, Nature 567 (2019) 76–80.
[52] T. Feng, X. Ruan, Four-phonon scattering reduces intrinsic thermal conductivity of graphene and the contributions from flexural phonons, Phys. Rev. B 97 (2018) 045202.
[53] C. Zhang, J. Sun, Y. Shen, W. Kang, Q. Wang, Effect of high order phonon scattering on the thermal conductivity and its response to strain of a penta-NiN_2 Sheet, J. Phys. Chem. Lett 13 (2022) 5734–5741.
[54] Y. Xia, V. Ozoliņš, C. Wolverton, Microscopic mechanisms of glasslike lattice thermal transport in cubic $Cu_{12}Sb_4S_{13}$ tetrahedrites, Phys. Rev. Lett. 125 (2020) 085901.
[55] J. Sun, C. Zhang, Z. Yang, Y. Shen, M. Hu, Q. Wang, Four-phonon scattering effect and two-channel thermal transport in two-dimensional paraelectric SnSe, ACS Appl. Mater. Interfaces 14 (2022) 11493–11499.
[56] Z. Liu, X. Wu, V. Varshney, J. Lee, G. Qin, M. Hu, A.K. Roy, T. Luo, Bond saturation significantly enhances thermal energy transport in two-dimensional pentagonal materials, Nano Energy 45 (2017) 1–9.
[57] H. Liu, G. Qin, Y. Lin, M. Hu, Disparate strain dependent thermal conductivity of two-dimensional penta-structures, Nano Lett. 16 (2016) 3831–3842.
[58] J. Sun, Y. Guo, Q. Wang, Y. Kawazoe, Thermal transport properties of penta-graphene with grain boundaries, Carbon 145 (2019) 445–451.